

3D phase diversity: a myopic deconvolution method for short-exposure images: application to retinal imaging

Guillaume Chenegros and Laurent M. Mugnier

Department of Optics, Office National d'Études et de Recherches Aérospatiales, BP 72, F-92322 Châtillon Cedex, France

François Lacombe

Mauna Kea Technologies, 9 rue d'Enghien, 75010 Paris, France

Marie Glanc

Laboratoire d'Études Spatiales et d'Instrumentation en Astrophysique, Observatoire de Paris-Meudon, 5 place Jules Janssen, 92195 Meudon Cedex, France

Received July 31, 2006; revised October 2, 2006; accepted October 3, 2006;
posted October 10, 2006 (Doc. ID 73587); published April 11, 2007

3D deconvolution is an established technique in microscopy that may be useful for low-cost high-resolution imaging of the retina. We report on a myopic 3D deconvolution method developed in a Bayesian framework. This method uses a 3D imaging model, a noise model that accounts for both photon and detector noises, a regularization term that is appropriate for objects that are a mix of sharp edges and smooth areas, a positivity constraint, and a smart parameterization of the point-spread function (PSF) by the pupil phase. It estimates the object and the PSF jointly. The PSF parameterization through the pupil phase constrains the inversion by dramatically reducing the number of unknowns. The joint deconvolution is further constrained by an additional longitudinal support constraint derived from a 3D interpretation of the phase-diversity technique. This method is validated by simulated retinal images. © 2007 Optical Society of America

OCIS codes: 100.1830, 100.3020, 100.5070, 100.6890, 170.6900, 010.1080.

1. INTRODUCTION

Early detection of pathologies of the human retina calls for an *in vivo* exploration of the retina at the cell scale. Direct observation from the outside suffers from the poor optical quality of the eye. The time-varying aberrations of the eye can be compensated *a posteriori* if measured simultaneously with the image acquisition; this technique is known as deconvolution from wavefront sensing^{1,2} and has been successfully applied to the human retina.³ These aberrations can also be compensated for in real time by use of adaptive optics⁴ (AO). Yet, the correction is always partial.^{5–7} Additionally, the object under examination (the retina) is three dimensional (3D), and each recorded image contains contributions from the whole object's volume.

In two-dimensional (2D) deconvolution, each image is deconvolved separately; i.e., only one object plane is assumed to contribute to each image. This is an appropriate image model in astronomy, for instance, but is a somewhat crude approximation in microscopy, as it does not properly account for the halo in each image that comes from the parts of the observed object that are out of focus.

Three-dimensional deconvolution is an established technique in microscopy and, in particular, in conventional fluorescence microscopy.⁸ The combination of a con-

ventional microscope with deconvolution is often referred to as deconvolution microscopy or even “digital confocal,” because the use of 3D deconvolution can notably improve the resolution of the recorded conventional images, especially in the longitudinal dimension, while remaining simpler and cheaper than a confocal microscope.

Yet, to the best of our knowledge, deconvolution of retinal images has so far been performed with 2D deconvolution techniques, both in deconvolution from wavefront sensing³ and in deconvolution of AO-corrected images.⁹

Besides, because deconvolution is an ill-posed inverse problem,^{10–12} most modern deconvolution methods use regularization in order to avoid an uncontrolled amplification of the noise. The regularization that is commonly used in 3D deconvolution is the classical Tikhonov regularization, which is quadratic (see Subsection 2.B) and thus tends to oversmooth edges. In Section 3 we present a regularized edge-preserving 3D deconvolution method.

Furthermore, a deconvolution method needs a precise estimate of the point-spread function (PSF), which is not always available. This is particularly true for 3D imaging. We thus propose a myopic deconvolution method that estimates simultaneously the PSF and the object in Section 3.

To better constrain the problem, we propose the use of

an additional constraint in Section 5. The efficiency of this proposed constraint is shown on realistic simulated retinal images.

2. 3D DECONVOLUTION METHOD WITH KNOWN PSF

A. Imaging Model

The image formation is modeled as a 3D convolution:

$$\mathbf{i} = \mathbf{h} * \mathbf{o} + \mathbf{n},$$

where \mathbf{i} is the (3D) pile of (2D) recorded images, \mathbf{o} is the 3D unknown observed object that concatenates each object slice (which slices are regularly spaced out of δz), \mathbf{h} is the 3D PSF, \mathbf{n} is the noise, and $*$ denotes the 3D convolution operator. For a system with N images of N object planes, this 3D convolution can be rewritten as

$$\mathbf{i}_k = \left(\sum_{l=0}^{N-1} \mathbf{h}_{k-l} * \mathbf{o}_l \right) + \mathbf{n}_k, \quad (1)$$

where \mathbf{o}_j is the object in plane j , \mathbf{i}_k is the k th recorded image, and \mathbf{h}_{k-j} is the 2D PSF corresponding to a defocus of $(k-j)\delta z$. The PSF is that of the system composed of the eye, the imaging system (including the AO); and the detector. We assume that the whole recording process is fast enough that the different 2D PSFs differ only by a defocus (see Section 3). Figure 1 illustrates the imaging process in the case of three object and image planes.

B. 3D Deconvolution Method

Most deconvolution techniques boil down to the minimization (or maximization) of a criterion. An important task is the definition of a suitable criterion for the given inverse problem.

Following the Bayesian¹² maximum *a posteriori* (MAP) approach, the deconvolution problem can be stated as follows: we look for the most likely object $\hat{\mathbf{o}}$, given the observed image \mathbf{i} and our prior information on \mathbf{o} , which is summarized by a probability density $p(\mathbf{o})$. This reads as

$$\hat{\mathbf{o}} = \underset{\mathbf{o}}{\arg \max} p(\mathbf{o}|\mathbf{i}) = \underset{\mathbf{o}}{\arg \max} p(\mathbf{i}|\mathbf{o}) \times p(\mathbf{o}).$$

Equivalently, $\hat{\mathbf{o}}$ can be defined as the object that minimizes a compound criterion $J(\mathbf{o})$ defined as follows:

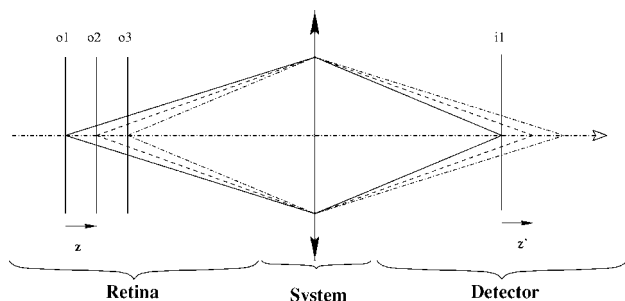


Fig. 1. Illustration of the 3D image formation for three object planes. The object is on the left, and the image is on the right. The system is composed of the eye and the optical system (including the AO). In image i_1 , object o_1 is focused; o_2 and o_3 are defocused. Images i_2 and i_3 are not represented here.

$$J(\mathbf{o}) = J_i(\mathbf{o}) + J_o(\mathbf{o}),$$

where the negative log likelihood $J_i = -\ln p(\mathbf{i}|\mathbf{o})$ is a measure of fidelity to the data and $J_o = -\ln p(\mathbf{o})$ is a regularization or penalty term, so the MAP solution can equivalently be called a penalized-likelihood solution.

The noise is a mixture of nonstationary, Poisson-distributed photon noise and detector noise, which can be reasonably modeled as nonstationary white Gaussian as soon as the flux level is a few tens of photoelectrons per pixel.¹³ If the noise statistics are additive, nonstationary white Gaussian, then the data fidelity term is a simple weighted least-squares difference between the actual data \mathbf{i} and our model of the data for a given object, $\mathbf{h} * \mathbf{o}$:

$$J_i(\mathbf{o}) = \frac{1}{2} \sum_{k=0}^{N-1} \sum_{p,q=0}^{N_{pix}-1} \left(\frac{1}{\sigma_k^2(p,q)} \left| \mathbf{i}_k(p,q) - \sum_{l=0}^{N-1} (\mathbf{h}_{k-l}(p,q) * \mathbf{o}_l(p,q)) \right|^2 \right), \quad (2)$$

where $\sigma_k(p,q)$ is the noise variance in the layer k for the pixel (p,q) .

C. Object Prior

The choice of a Gaussian prior probability distribution for the object can be justified from an information theory standpoint as being the least informative, given the first two moments of the distribution. In this case, a reasonable model of the object's power spectral density (PSD) can be found¹⁴ and used to derive the regularization criterion J_o , which is then quadratic (or L_2 for short). The chosen PSD model is

$$\text{PSD}(f) = E[|\mathbf{o}(f)|^2] - |\mathbf{o}_m(f)|^2 = k/[1 + (f/f_0)^p] - |\mathbf{o}_m(f)|^2,$$

where f is the spatial frequency, \mathbf{o}_m is the *a priori* object (it is typically a constant), p characterizes the regularity of the object, and f_0 is a cutoff frequency introduced to avoid the divergence at the origin and is typically the inverse of the characteristic size of the image. Additionally, the parameters of the object's PSD can be estimated automatically (i.e., in an unsupervised way) from the data by a maximum-likelihood method¹⁵ derived from the method developed by Blanc *et al.*¹⁶ in the phase-diversity context.

The disadvantage of a Gaussian prior (or, equivalently, of a quadratic regularization term), especially for objects with sharp edges such as photoreceptors or vessels, is that it tends to oversmooth edges. A possible remedy is to use an edge-preserving prior that is quadratic for small gradients and linear for large ones.¹⁷ The quadratic part ensures a good smoothing of the small gradients (i.e., of noise), and the linear behavior cancels the penalization of large gradients (i.e., of edges), as explained by Bouman and Sauer.¹⁸ Such priors are called quadratic-linear, or L_2 - L_1 for short.¹⁹ Here we use a function that is an isotropic version of the expression suggested by Rey²⁰ in the context of robust estimation, used by Brette and Idier²¹ for image restoration, and recently applied to imaging through turbulence.^{2,13} The choice of the crossover point from L_2 to L_1 is currently supervised and performed as

explained by Mugnier *et al.*¹³ It is typically of the order of the mean difference between adjacent pixels in the image.

The functional J_o is strictly convex, and J_i of Eq. (2) is convex because it is quadratic, so that the global criterion $J=J_i+J_o$ is strictly convex. This ensures uniqueness and stability of the solution with respect to noise and also justifies the use of a gradient-based method for the minimization.

3. MYOPIC 3D DECONVOLUTION

In this section we address the case where the PSF \mathbf{h} is not known precisely. An approach that has proven effective for 2D imaging is myopic deconvolution, i.e., performing a joint estimation of the object \mathbf{o} and the PSF \mathbf{h} . Unfortunately, for an N -plane 3D object and 3D image, the 3D PSF is composed of $2N-1$ layers. The problem is more underdetermined than in two dimensions. Furthermore, this method does not make use of the strong relationship between PSF planes: the different 2D PSFs differ only by a defocus. Because we have short-exposure images, we can parameterize the whole 3D PSF by a common pupil phase φ plus a known defocus phase that depends on the considered PSF plane. This has been already used for short-exposure 2D imaging through atmospheric turbulence.^{2,22,23} This dramatically reduces the number of unknowns (we assume that we know the distance between two layers). Additionally, the pupil phase is expanded on Zernike polynomials (as defined by Noll²⁴) so that at most a few tens of coefficients are required to describe the 3D PSF:

$$h_k(\varphi) = |\text{FT}^{-1}\{P(x,y)\exp(j(\varphi(x,y) + \varphi_d^k(x,y)))\}|^2, \\ \varphi(x,y) = \sum_{m=5}^M \alpha_m Z_m(x,y), \quad (3)$$

where P is the pupil function and φ_d^k corresponds to the defocus phase of layer k . φ is the unknown pupil phase, and $j^2=-1$. This defocus phase is calculated with

$$\varphi_d^k(x,y, \delta z) = \alpha_4^d(\delta z) \cdot Z_4(x,y),$$

where

$$\alpha_4^d(\delta z) = \pi \cdot \frac{\delta z}{8 \cdot \sqrt{3} \cdot \frac{\lambda}{n} \cdot \left(\frac{f \cdot n}{D}\right)^2},$$

where λ is the imaging wavelength in the air, n is the refractive index, f is the focal distance of the eye in the air, and D is the pupil diameter.

We jointly estimate the 3D object and the pupil phase in the same MAP framework. This joint MAP estimator is

$$[\hat{\mathbf{o}}, \hat{\varphi}] = \arg \max_{\mathbf{o}, \varphi} p(\mathbf{o}, \varphi | \mathbf{i}) = \arg \max_{\mathbf{o}, \varphi} p(\mathbf{i} | \mathbf{o}, \varphi) \times p(\mathbf{o}) \times p(\varphi).$$

Equivalently, $\hat{\mathbf{o}}$ and $\hat{\varphi}$ can be defined as the object and the phase that minimize a compound criterion $J(\mathbf{o}, \varphi)$ defined as follows:

$$J(\mathbf{o}, \varphi) = J_i(\mathbf{o}, \varphi) + J_o(\mathbf{o}) + J_\varphi(\varphi), \quad (4)$$

where $J_i = -\ln p(\mathbf{i} | \mathbf{o}, \varphi)$ is the negative log likelihood and is given by Eq. (2), except that now it is considered a function of \mathbf{o} and φ . $J_o(\mathbf{o}) = -\ln p(\mathbf{o})$ is a $L2$ or $L2-L1$ regularization criterion (see Subsection 2.C). We assume a Gaussian probability density function for φ , so $J_\varphi(\varphi) = -\ln p(\varphi)$ is a regularization criterion on the phase defined by

$$J_\varphi(\varphi) = \frac{1}{2}(\varphi - \bar{\varphi})^t C_\varphi^{-1}(\varphi - \bar{\varphi}),$$

where $\bar{\varphi}$ is the *a priori* phase mean (usually zero) and C_φ is the *a priori* phase covariance matrix. Additionally, because the images considered here are illuminated rather uniformly (due to all the out-of-focus object planes contributing to each image), stationary white Gaussian statistics, with a constant variance equal to the mean number of photoelectrons per pixel, is a reasonable approximation for the noise model, so that J_i simplifies to

$$J_i(\mathbf{o}, \varphi) = \frac{1}{2\sigma_n^2} \sum_{k=0}^{N-1} \left\| \mathbf{i}_k - \sum_{l=0}^{N1} (\mathbf{h}_{k-l}(\varphi) * \mathbf{o}_l) \right\|^2.$$

The criterion $J(\mathbf{o}, \varphi)$ of Eq. (4) is minimized numerically on \mathbf{o} and φ . The minimization is performed by the optimization variable metric with limited memory and bounds (OP-VMLMB) method, designed by Thiébaud.²⁵ This method is faster than the conjugate-gradient method.

The simplest way to organize the unknowns for the minimization is to stack the object and the phase together into a vector and to run the OP-VMLMB routine on this variable. Yet, this can be slow as the gradients of the criterion with respect to the object and to the phase may have different orders of magnitude. We have found that the minimization is speeded up by splitting it into two blocks and alternating between minimizations on the object for the current phase estimate and minimizations on the phase for the current object estimate.

The minimization starts by estimating the object for a fixed (zero) phase. The initial guess for the object is, for instance, the image itself. The minimization is not stopped by hand but, rather, when the estimated object and phase no longer evolve (i.e., when their evolution from one iteration to the next is close to machine precision).

4. VALIDATION BY SIMULATIONS AND LIMITATIONS

A. Simulations

To validate our deconvolution method by simulations, we created a simulated object that complies with the overall structure of a retina. Figure 2 represents the original simulated object, composed of vessels, ganglion cells, and photoreceptors. The vessels are simulated by moving a ring in a random walk, the ganglion cells are simulated by empty globes, and photoreceptors are represented by two empty half-spheres joined by an empty tube. The cube's height on Fig. 2 is approximative $52 \mu\text{m}$, and the depth and the width of this cube are 300 pixels.

In the simulations presented here, we use a five-slice object obtained by averaging the data from Fig. 2 into five

13 μm thick slices from which we select a 128×128 region of interest (the depth of focus is approximately 18 μm). The five slices obtained are presented on Fig. 3.

The PSFs used to compute the 3D image \mathbf{i} are currently purely diffractive (no multiple scattering). They are gen-

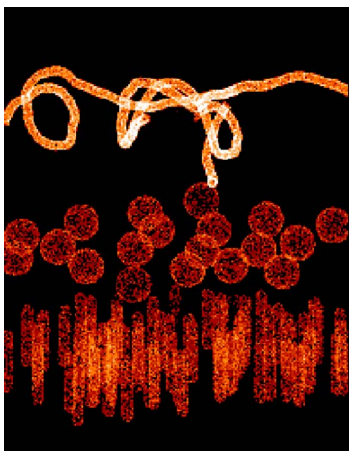


Fig. 2. (Color online) Perspective view of the 3D object used for the simulations.

erated with a set of aberrations expanded on the Zernike basis (the Z_i coefficients are normalized); we use 0.2 rd root-mean-square (RMS) on the aperture of astigmatism (Z_5), -0.1 rd RMS on the aperture of astigmatism (Z_6), and -0.5 rd RMS on the aperture of spherical aberration (Z_{11}). These PSFs are oversampled (with respect to the Nyquist frequency) by a factor of 1.5. With the object and the PSF, we simulate the image by means of Eq. (1). The noise added is white Gaussian and stationary; its standard deviation is 3% of the maximum intensity in the object \mathbf{o} (corresponding roughly to 1000 photoelectrons per pixel (ph/pix) for photon-limited data). The five image layers are presented on Fig. 4. From these images, it is clear that all object slices contribute to all images. With the relatively small chosen separation between planes (13 μm), the first two images are visually identical, whereas the corresponding object slices are very different. The deconvolution aims at disentangling the contribution of each object slice and improving the resolution within each plane.

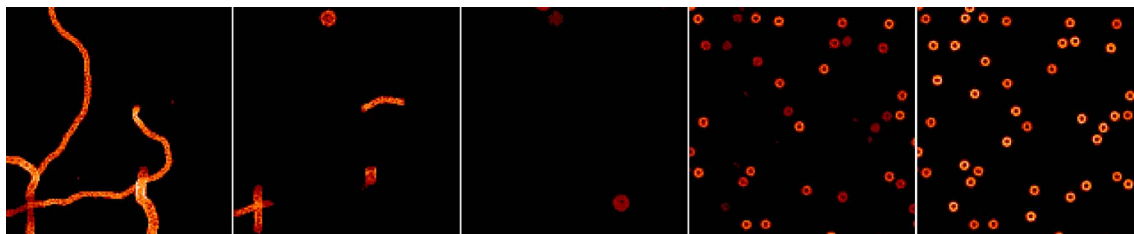


Fig. 3. (Color online) Five object layers [black corresponds to 0 photoelectrons per pixel (ph/pix)].

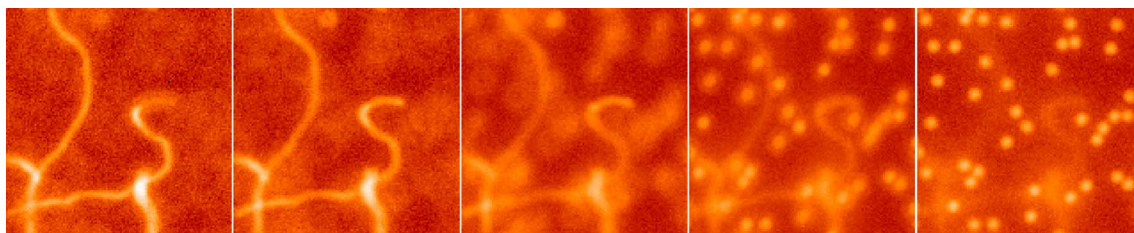


Fig. 4. (Color online) Five image layers.

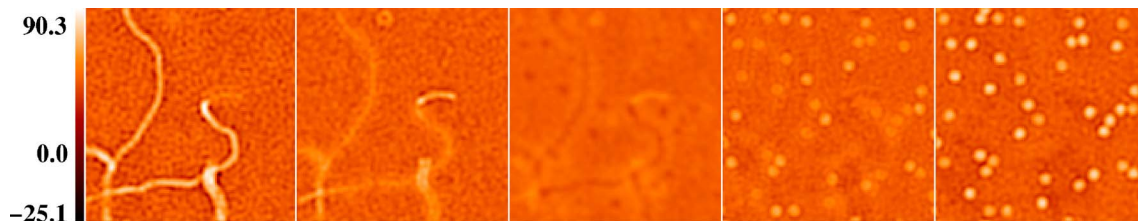


Fig. 5. (Color online) Five estimated object layers with L_2 regularization without the positivity constraint and using the true PSF.

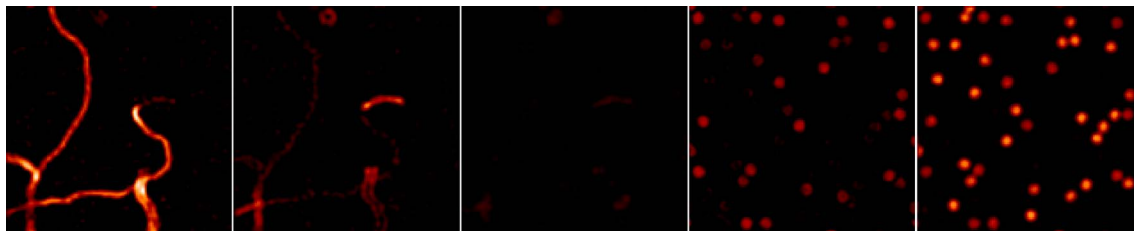


Fig. 6. (Color online) Five estimated object layers with L_2 regularization under the positivity constraint and using the true PSF (black corresponds to 0 ph/pix).



Fig. 7. (Color online) Five estimated object layers with $L2-L1$ regularization under the positivity constraint and using the true PSF (black corresponds to 0 ph/pix).

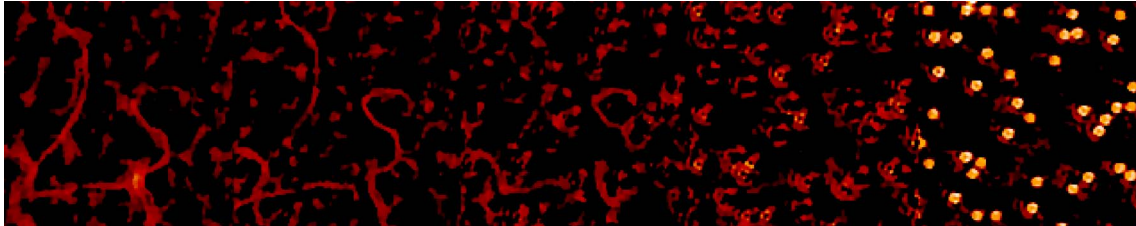


Fig. 8. (Color online) Deconvolution with a wrong (unaberrated) PSF. The different object planes are not correctly disentangled because of the mismatch between true PSF and assumed PSF (black corresponds to 0 ph/pix).

B. Deconvolution with Known PSF

In this subsection, we present three results obtained with our deconvolution method and the two priors mentioned in Subsection 2.C. The first simulation, presented on Figs. 5 and 6, shows the deconvolution results obtained with $L2$ regularization without and with the positivity constraint, respectively. We can see ghosts of vessels (in the middle plane, for example) on Fig. 5 and a residual blur: the missing cone of 3D frequencies makes it difficult for the restoration procedure to correctly disentangle the contribution of all planes. Edges are not preserved ($L2$ regularization and no positivity constraint prevent spectral extrapolation). The positivity constraint used in Fig. 6 helps the algorithm disentangle the different planes and visibly reduces ghosts of vessels in the middle plane. More quantitatively, the RMS restoration error is 8.34 ph/pix with the positivity constraint and 10.31 ph/pix without (the object average level is 15.34 ph/pix). On Fig. 7 we present a deconvolution performed with $L2-L1$ regularization under the positivity constraint. The edges are much better preserved, and the separation between the different planes is also slightly better on the second restored image plane. The RMS restoration error is 6.33 ph/pix. To evaluate the need for precision in the PSF knowledge, we performed a deconvolution with a wrong (unaberrated) PSF shown in Fig. 8. The regularization used is $L2-L1$ under the positivity constraint, and the RMS restoration error is 11.28 ph/pix. On both Figs. 7 and 8, the lateral resolution is improved with respect to that of the images (Fig. 4). But only on Fig. 7 are the object planes correctly disentangled. In other words, the longitudinal resolution is very poor in Fig. 8 due to the mismatch between the true PSF and the one assumed for the deconvolution.

C. Results with the Myopic Method

We present here the estimated aberrations (see Fig. 9) with the myopic method [joint estimation of \mathbf{o} and φ by minimization of criterion $J(\mathbf{o}, \varphi)$ of Eq. (4)]. The true pupil phase standard deviation is $\sigma_\varphi = 0.53$ rd, and the RMS error with the positivity constraint is $\sigma_\varepsilon = 0.24$ rd. Without

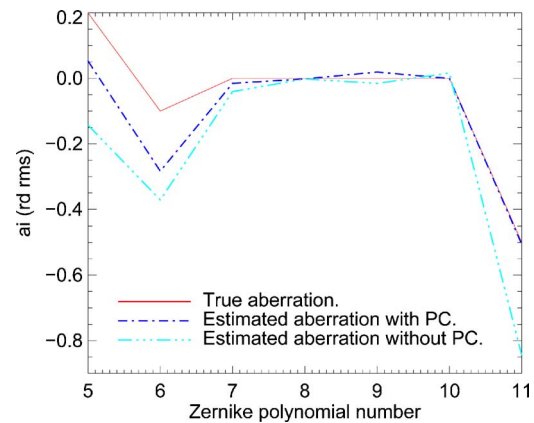


Fig. 9. (Color online) Estimated aberrations with and without the positivity constraint (PC).

the positivity constraint, the RMS error is $\sigma_\varepsilon = 0.56$ rd. The estimated phase without the positivity constraint cannot reasonably be used to deconvolve images. A likely explanation for the poor results of the method without the positivity constraint is that the criterion may have several minima. It has been shown in Subsection 2.C that the criterion $J(\mathbf{o}, \varphi)$ is strictly convex for any given φ so there exists a unique object solution for a given set of aberrations φ , denoted by $\hat{\mathbf{o}}(\varphi) : \hat{\mathbf{o}}(\varphi) = \arg \min_{\mathbf{o}} J(\mathbf{o}, \varphi)$. To validate the hypothesis of a nonconvex criterion, we define a partially optimized criterion as $J'(\varphi) \triangleq J(\hat{\mathbf{o}}(\varphi), \varphi)$, and we perform a plot of this criterion. If several minima are found on φ for J' , then it is the unambiguous sign of the existence of several minima on (\mathbf{o}, φ) for the criterion $J(\mathbf{o}, \varphi) : \hat{\varphi} = \arg \min_{\varphi} J'(\varphi) \Leftrightarrow (\hat{\mathbf{o}}(\hat{\varphi}), \hat{\varphi}) = \arg \min_{\mathbf{o}, \varphi} J(\mathbf{o}, \varphi)$. The plots of the values of $J'(\varphi)$ (computed for a grid of a_5 and a_6 values taken between -1 rd and 1 rd and for the true values of the other aberrations) are presented in Figs. 10 and 11. The criterion plotted on Fig. 11 without the positivity constraint presents several minima and is obviously nonconvex, whereas the one obtained with the positivity constraint plotted on Fig. 10 shows a global minimum that is close to the true aberrations.

tions. In this case at least, the positivity constraint restricts the solution space to a unique solution to the minimization problem.

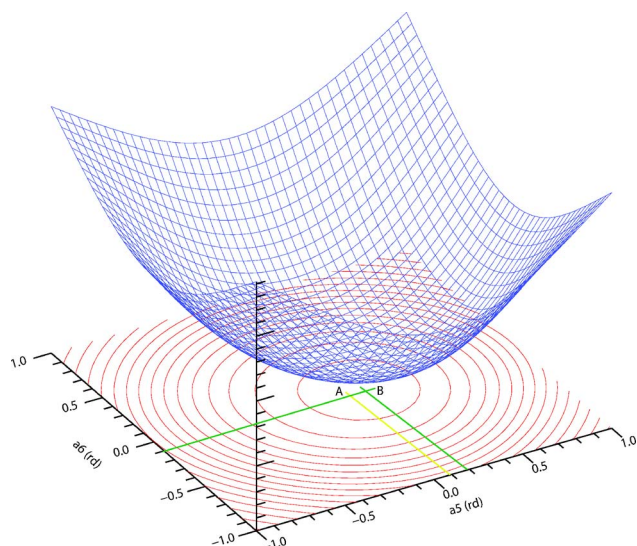


Fig. 10. (Color online) Criterion surface with the positivity constraint: the criterion is strictly convex. *A* is the position of the global minimum; it is close to the position of the true aberrations *B*.

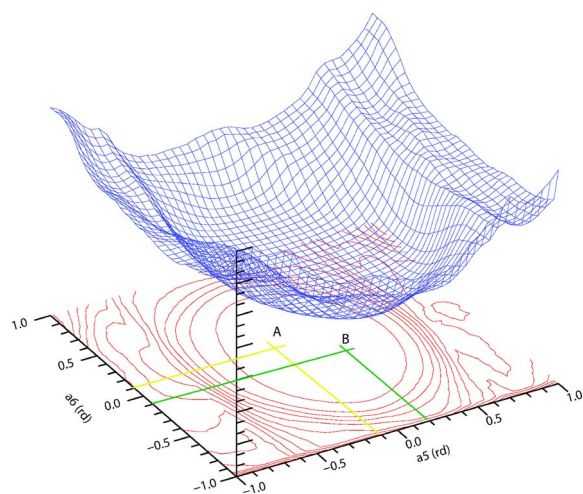


Fig. 11. (Color online) Criterion surface without the positivity constraint: the criterion is nonconvex. *A* is the position of the global minimum, and *B* is the position of the true aberrations.

For an object with a background, the positivity constraint becomes less and less effective as the background level increases. For a very high background, the deconvolution tends to the one obtained on Fig. 11 without the positivity constraint, as checked by earlier simulation.²⁶ Because the positivity constraint is not always effective, we wish to find another, more effective, constraint in order to improve the phase estimation.

5. PHASE DIVERSITY

We first briefly present the classical phase-diversity wavefront sensing technique and the case in which it is used. Then we introduce our 3D extension of it, and we validate it with some simulations.

A. Conventional Phase Diversity

Phase diversity is a focal-plane wavefront sensing technique proposed by Gonsalves²⁷ (see Ref. 28 for a review), which uses two (or more) images close to a focal plane to estimate the aberrations of an optical instrument. These two images (as shown on Fig. 12) differ by a known aberration (for instance, defocus) in order to estimate the pupil phase via a criterion minimization.

The two images recorded on the imaging camera are the convolution of the object by the PSF plus photon and detector noises. As shown in Eqs. (5), there is a nonlinear relation between the PSF and the parameter of interest φ :

$$i_f = h(\varphi) * o + n,$$

$$i_d = h(\varphi + \varphi_d) * o + n, \quad (5)$$

where h is defined in Eq. (3), φ is the phase, φ_d is the known aberration, o is the observed object, n is the noise, and $*$ stands for the convolution process.

B. 3D Phase Diversity

Despite the fact that the myopic method described in Section 3 uses a 3D imaging model, that it uses a PSF model parameterized by the pupil phase (only a few tens of Zernike coefficients are required to describe the 3D PSF), and that it uses the positivity constraint, the precision obtained on estimated aberrations is modest (see Fig. 9). Furthermore, the estimation of aberrations without the positivity constraint is unacceptable. A reinterpretation of 2D phase diversity, classically used with opaque objects,

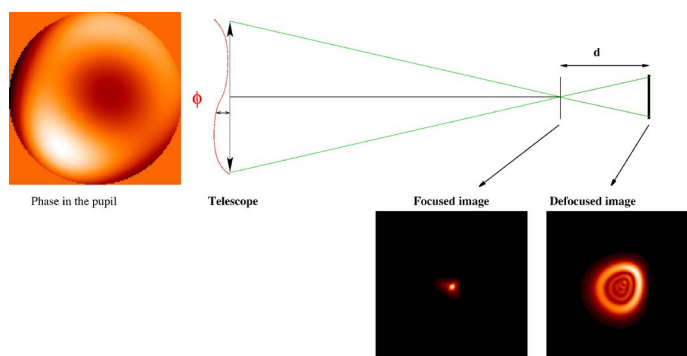


Fig. 12. (Color online) Principle of phase diversity: two images differing by a known aberration (here defocus) are used to estimate the pupil phase.

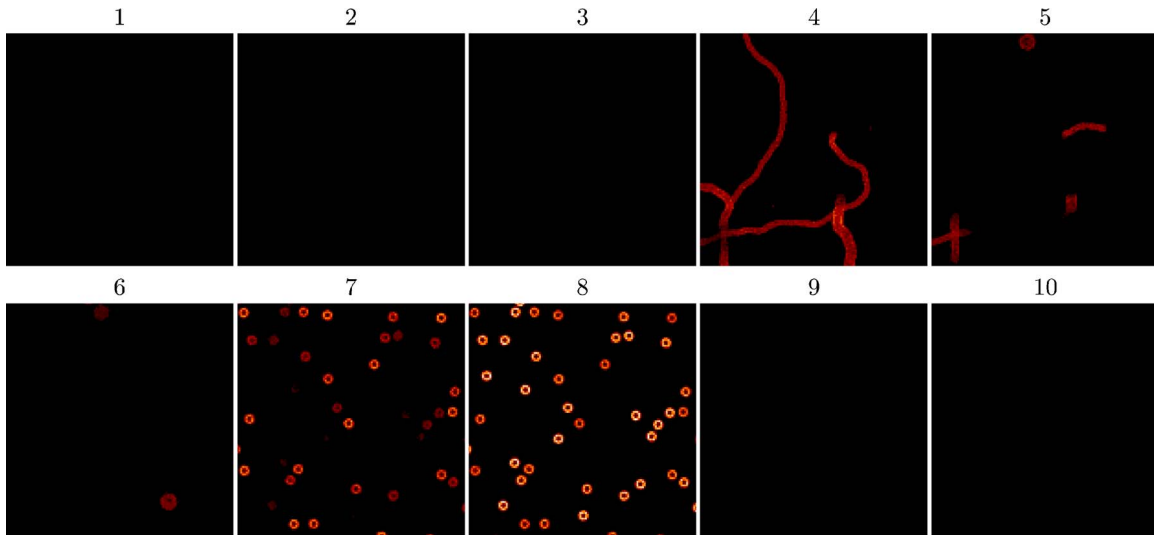


Fig. 13. (Color online) Ten object layers where five layers are empty (black corresponds to 0 ph/pix).

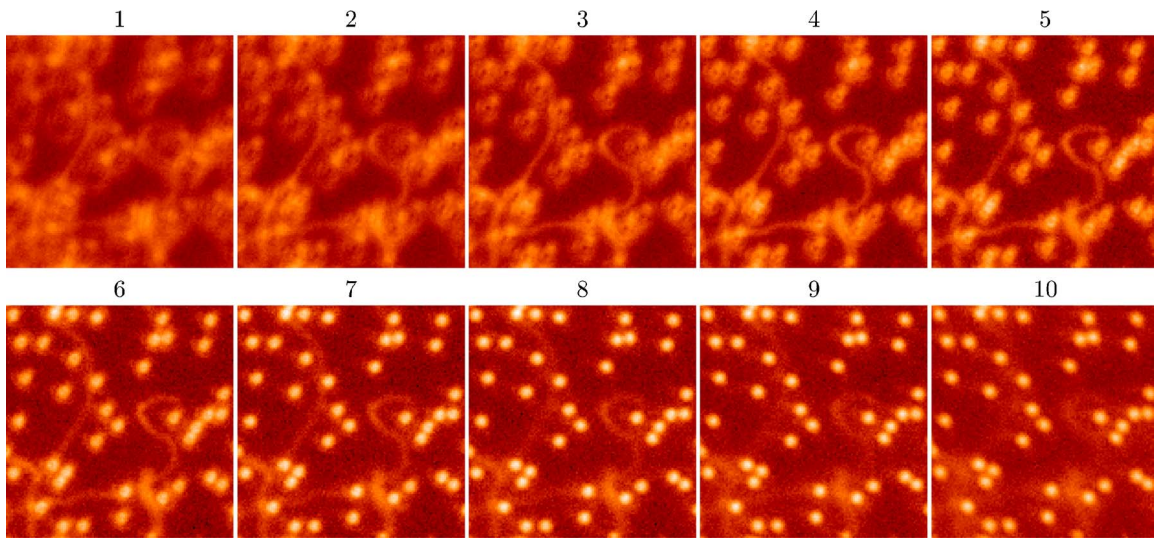


Fig. 14. (Color online) Ten simulated image layers.

is that only one out of the two image planes contains an object. In contrast, the myopic deconvolution used so far in this paper uses as many object planes as there are images. This 3D interpretation of conventional phase diversity prompts us to use a few additional images focused before (and possibly after) the object of interest. Furthermore, in the eye, we can indeed easily record images with no object (images focused in the vitreous, for instance). We assume and impose that some \mathbf{o} planes are empty (see Fig. 13) and call this the Z support constraint. This additional prior knowledge is a strong constraint for the phase inversion, which makes the positivity constraint unnecessary at least in the conditions of the simulations presented below. The criterion of fidelity to the data $J_i(\mathbf{o}, \varphi)$ (see Section 3) becomes

$$J_i(\mathbf{o}, \varphi) = \frac{1}{2\sigma_n^2} \sum_{k=0}^{N-1} \left\| \mathbf{i}_k - \sum_{\substack{t=0 \\ l \in S_o}}^{N-1} (\mathbf{h}_{k-t}(\varphi) * \mathbf{o}_l) \right\|^2,$$

where S_o is the list of nonempty object plane numbers. Typically, $S_o = [l_{min}, l_{max}]$ with $l_{min} \geq 0$ and $l_{max} \leq N-1$.

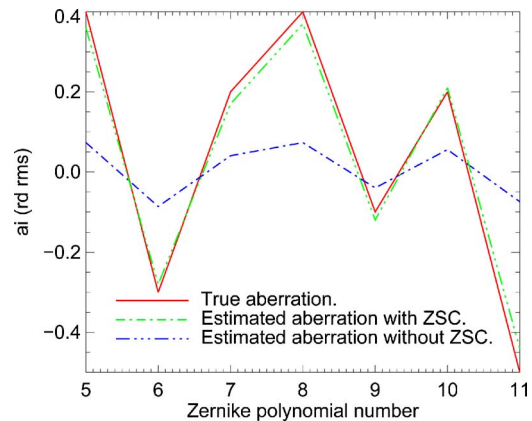


Fig. 15. (Color online) Estimated aberrations with and without the Z support constraint (ZSC).

The 3D imaging performed on an opaque 3D object can use a hard constraint: for any (x,y) , at most one object voxel $[x,y,z(x,y)]$ re-emits the light because of the object opacity.^{29,30} In our case, which is 3D imaging performed



Fig. 16. (Color online) Five estimated object layers with $L2-L1$ regularization under the positivity constraint and ZSC (black corresponds to 0 ph/pix).

on a translucent object (the retina), such an opacity constraint is inappropriate. That is why we propose the Z support constraint, which can be expressed as $\mathbf{o}(x,y,z) = 0 \forall z \in [z_{min}, z_{max}]$.

C. Validation by Simulations

To validate the efficiency of the Z support constraint, we performed numerous simulations, of which one is presented here.

The simulation conditions (noise, distance between two planes, PSF oversampling) are the same as in Subsection 4.A except that the aberrations are stronger to test the 3D phase-diversity method. The object \mathbf{o} is composed of five layers with the object (the same as in Subsection 4.A) and five without (see Fig. 13). The ten image layers are presented on Fig. 14. The true pupil phase standard deviation is $\sigma_\phi = 0.87$ rd. The results are presented in Fig. 15: the RMS error with the Z support constraint is only $\sigma_\varepsilon = 0.088$ rd. Without the Z support constraint, the RMS error is $\sigma_\varepsilon = 0.70$ rd, which is unacceptable. The phase estimation with the Z support constraint is precise enough to correctly deconvolve images: the deconvolution result (with this estimated phase) is given in Fig. 16. The RMS restoration error is 6.68 ph/pix with $L2-L1$ regularization under the positivity constraint and Z support constraint. We have checked that if we use the true PSF and $L2-L1$ regularization under the positivity constraint (the RMS restoration error is 6.33 ph/pix, see Subsection 4.B) instead of the one estimated with $L2-L1$ regularization under the positivity constraint and Z support constraint, we obtain a restored object that is visually identical to that of Fig. 16.

6. CONCLUSION AND PERSPECTIVES

A myopic 3D deconvolution method has been developed in a Bayesian framework. It uses a 3D imaging model, a fine noise model, an appropriate regularization term, and a parameterization of the point-spread function via the pupil phase. To improve the deconvolution performance, in particular for cases when the positivity constraint on the object is not effective (object with background), we have proposed the use of 3D phase diversity. This consists of recording additional images focused before (and possibly after) the object of interest and adding the corresponding longitudinal (Z) support constraint to the deconvolution. This can be very appropriate in particular for retinal images. We have demonstrated the effectiveness of the method and, in particular, of the Z support constraint on realistic simulated data.

To check the robustness of our myopic deconvolution method with respect to imperfections in the imaging model, a definitive validation should be performed on experimental data; this will constitute the next step of our work.

The corresponding author's e-mail address is Guillaume.Chenegros@onera.fr.

REFERENCES

1. J. Primot, G. Rousset, and J.-C. Fontanella, "Deconvolution from wave-front sensing: a new technique for compensating turbulence-degraded images," *J. Opt. Soc. Am. A* **7**, 1598–1608 (1990).
2. L. M. Mugnier, C. Robert, J.-M. Conan, V. Michau, and S. Salem, "Myopic deconvolution from wave-front sensing," *J. Opt. Soc. Am. A* **18**, 862–872 (2001).
3. D. Catlin and C. Dainty, "High-resolution imaging of the human retina with a Fourier deconvolution technique," *J. Opt. Soc. Am. A* **19**, 1515–1523 (2002).
4. G. Rousset, J.-C. Fontanella, P. Kern, P. Gigan, F. Rigaut, P. Léna, C. Boyer, P. Jagourel, J.-P. Gaffard, and F. Merkle, "First diffraction-limited astronomical images with adaptive optics," *Astron. Astrophys.* **230**, 29–32 (1990).
5. M. C. Roggemann, "Limited degree-of-freedom adaptive optics and image reconstruction," *Appl. Opt.* **30**, 4227–4233 (1991).
6. J. M. Conan, P. Y. Madec, and G. Rousset, "Image formation in adaptive optics partial correction," in *Active and Adaptive Optics*, F. Merkle, ed., Vol. 48 of ESO Conference and Workshop Proceeding (European Southern Observatory/International Commission of Optics, 1994).
7. J.-M. Conan, "Étude de la correction partielle en optique adaptative," Ph.D. thesis (Université Paris XI, 1994).
8. J. G. McNally, T. Karpova, J. Cooper, and J. A. Conchello, "Three-dimensional imaging by deconvolution microscopy," *Methods* **19**, 373–385 (1999).
9. J. C. Christou, A. Roorda, and D. R. Williams, "Deconvolution of adaptive optics retinal images," *J. Opt. Soc. Am. A* **21**, 1393–1401 (2004).
10. A. Tikhonov and V. Arsenin, *Solutions of Ill-Posed Problems* (Winston, 1977).
11. G. Demoment, "Image reconstruction and restoration: overview of common estimation structures and problems," *IEEE Trans. Acoust., Speech, Signal Process.* **37**, 2024–2036 (1989).
12. J. Idier, ed., *Approche Bayésienne pour les Problèmes Inverses* (Hermès, 2001).
13. L. M. Mugnier, T. Fusco, and J.-M. Conan, "MISTRAL: a myopic edge-preserving image restoration method, with application to astronomical adaptive optics-corrected long-exposure images," *J. Opt. Soc. Am. A* **21**, 1841–1854 (2004).
14. J.-M. Conan, L. M. Mugnier, T. Fusco, V. Michau, and G. Rousset, "Myopic deconvolution of adaptive optics images by use of object and point-spread function power spectra," *Appl. Opt.* **37**, 4614–4622 (1998).
15. D. Gratadour, D. Rouan, L. M. Mugnier, T. Fusco, Y. Clénet, E. Gendron, and F. Lacombe, "Near-infrared

- adaptive optics dissection of the core of NGC 1068 with NaCo," *Astron. Astrophys.* **446**, 813–825 (2006).
16. A. Blanc, L. M. Mugnier, and J. Idier, "Marginal estimation of aberrations and image restoration by use of phase diversity," *J. Opt. Soc. Am. A* **20**, 1035–1045 (2003).
 17. P. J. Green, "Bayesian reconstructions from emission tomography data using a modified EM algorithm," *IEEE Trans. Med. Imaging* **9**, 84–93 (1990).
 18. C. Bouman and K. Sauer, "A generalized Gaussian image model for edge-preserving MAP estimation," *IEEE Trans. Image Process.* **2**, 296–310 (1993).
 19. J. Idier and L. Blanc-Féraud, "Deconvolution en imagerie," in *Approche Bayésienne pour les Problèmes Inverses*, J. Idier, ed. (Hermès, 2001), Chap. 6.
 20. W. J. J. Rey, *Introduction to Robust and Quasi-Robust Statistical Methods* (Springer-Verlag, 1983).
 21. S. Brette and J. Idier, "Optimized single site update algorithms for image deblurring," in *Proceedings of the International Conference on Image Processing* (IEEE Computer Society, 1996), pp. 65–68.
 22. T. J. Schulz, "Multiframe blind deconvolution of astronomical images," *J. Opt. Soc. Am. A* **10**, 1064–1073 (1993).
 23. E. Thiébaud and J.-M. Conan, "Strict *a priori* constraints for maximum-likelihood blind deconvolution," *J. Opt. Soc. Am. A* **12**, 485–492 (1995).
 24. R. J. Noll, "Zernike polynomials and atmospheric turbulence," *J. Opt. Soc. Am. A* **66**, 207–211 (1976).
 25. E. Thiébaud, "Optimization issues in blind deconvolution algorithms," in *Astronomical Data Analysis. II*, J.-L. Starck and F. D. Murtagh, eds., *Proc. SPIE* **4847**, 174–183 (2002).
 26. G. Chenegros, L. M. Mugnier, and F. Lacombe, "3D deconvolution of adaptive-optics corrected retinal images," in *Three-Dimensional and Multidimensional Microscopy: Image Acquisition and Processing XIII*, J.-A. Conchello, C. J. Cogswell, and T. Wilson, eds., *Proc. SPIE* **6090**, 60900P (2006).
 27. R. A. Gonsalves, "Phase retrieval and diversity in adaptive optics," *Opt. Eng.* **21**, 829–832 (1982).
 28. L. M. Mugnier, A. Blanc, and J. Idier, "Phase diversity: a technique for wave-front sensing and for diffraction-limited imaging," in *Advances in Imaging and Electron Physics*, P. Hawkes, ed. (Elsevier, 2006), Vol. 141, Chap. 1.
 29. M. F. Reiley, R. G. Paxman, J. R. Fienup, K. W. Gleichman, and J. C. Marron, "3D reconstruction of opaque objects from Fourier intensity data," in *Image Reconstruction and Restoration II*, T. J. Schulz, ed., *Proc. SPIE* **3170**, 76–87 (1997).
 30. R. G. Paxman, J. H. Seldin, J. R. Fienup, and J. C. Marron, "Use of an opacity constraint in three-dimensional imaging," in *Inverse Optics III*, M. A. Fiddy, ed., *Proc. SPIE* **2241**, 116–126 (1994).